Modeling present and future rock wall permafrost distribution in the Sisimiut mountain area, West Greenland

Marco Marcer[1,2], Pierre-Allain Duvillard[3,4], Soňa Tomaškovičová[1], Steffen Ringsø Nielsen[2,5], André Revil[4], and Thomas Ingeman-Nielsen[1]

[1]DTU Sustain,BygninRSTorvet, Bygning 115, 2800 Kgs. Lyngby, Denmark
[2]Arctic DTU, Siimuup Aqqutaa 32, B-1280, 3911 Sisimiut, Greenland
[3]NAGA Geophysics, 12 Allée du lac de Garde, Le Bourget du lac, France
[4]EDYTEM, Université Savoie Mont-Blanc, CNRS (UMR 5204), 73370 Le Bourget du Lac, France
[5]KTI Råstofskolen - Greenland School of Minerals and Petroleum, Adammip Aqq. 2, 3911 Sisimiut, Greenland

Correspondence: Marco Marcer (marcma@byg.dtu.dk)

Abstract. Rock wall permafrost is a feature of cold mountain ranges that was found responsible for the increase of rock fall and landslide activity in several regions across the globe. In Greenland, rock wall permafrost has received so far little attention from the scientific community, despite mountains are a predominant feature on the ice-free coastline and landslide activity is significant. With this study, we aim to move a first step towards the characterization of rock wall permafrost in Greenland. Our study area covers 100 km^2 of mountain terrain around the town of Sisimiut – 68° N on the West Coast. We first acquire ground surface temperature data for across the period 2020 - 2022 to model bedrock surface temperatures time series from weather forcing on the period 1850 - 2022. We then create weather forcing heat transfer transient simulations. In this way we obtain permafrost distribution maps and ad-hoc simulations for complex topographies. Our model results are compared to temperature data from two lowland boreholes (100 m depth) and geophysical data describing frozen/unfrozen conditions across a mid-elevation mountain ridge. Finally, we use regional carbon pathway scenarios 2.6 and 8.5 to evaluate future evolution of ground temperatures until the end of the 21st century. Our data and simulation describe discontinuous permafrost distribution in rock walls up to roughly 400 m.a.s.l.. Future scenarios suggest a decline of deep frozen bodies up to 800 m.a.s.l., i.e. the highest summits in the area. In summary, this study depicts a picture of warm permafrost in this area, highlighting its sensitivity to ongoing climate change.

1 Introduction

In cold mountain regions, complex topography influences shading, snow distribution and ground type, causing a highly variable distribution of ground temperatures and permafrost in steep rock walls (Etzelmüller, 2013). Several field studies describe a significant correlation between warming climate, rock wall permafrost degradation and increased slope instability, observed as rockfall frequency (Ravanel and Deline, 2011; Gallach et al., 2020) and large rockslide occurrence (Patton et al., 2019; Guerin et al., 2020; Frauenfelder et al., 2018; Walter et al., 2020). Therefore, understanding the spatial distribution of rock wall permafrost and its future evolution is a key step in defining potential hazard areas (GAPHAZ, 2017), and several countries

started comprehensive programs to monitor this phenomena as a basis for risk assessment (Pellet and Noetzli, 2020; Isaksen et al., 2022).

In Greenland, the scientific community still does not have a precise quantification of rock wall permafrost distribution. Available models are based on numerical simulations at kilometer scale (Brown, 1960; Daanen et al., 2011), are not calibrated with in-situ data (Gruber, 2012), or valid for sedimentary terrain only (Obu et al., 2019). Furthermore, our understanding of the evolution of mountain permafrost in the region is limited, as only Daanen et al. (2011) investigates future permafrost distribution, although at 25 km resolution. This knowledge gap poses a significant challenge to our comprehension of mountain hazards and their evolution, hindering the urgent need for a regional-scale hazard assessment in Greenland. This is particularly pressing due to the prevalence of landslides associated with permafrost degradation, as evidenced by prior studies (Svennevig, 2019; Svennevig et al., 2022, 2023; Walls et al., 2020), and the tangible impact of these events on the local population (Strzelecki et al., 2020).

The fact that ground temperature data in Greenland are limited to a few low-land sedimentary boreholes that are not representative for rock wall bedrock permafrost in complex terrain, is a major challenge for modelling this feature in this region. (Obu et al., 2019). A common strategy to overcome this issue is based on the approach developed in Switzerland in the early 2000's (Gruber et al., 2004) relying on a network of permanent surface temperature loggers. These data are used for transient modelling of ground temperatures across 1D profiles in relation with depth (Westermann et al., 2016), as well as in 2D (Magnin et al., 2017) and more complex 3D geometries (Noetzli et al., 2007). Several studies model ground temperatures using numerical approaches, as TEBAL (Stocker-Mittaz et al., 2002; Gruber et al., 2004) and CryoGrid (Myhra et al., 2017; Czekirda et al., 2023). Both models have a numerical approach to the evaluation of the Surface Energy Balance (SEB), i.e. the transfer from weather parameters to surface energy flux as upper boundary condition for the heat transfer module. Other studies have handled the SEB problem using an empirical approach based on correlating weather data and measured ground surface temperatures (Magnin et al., 2017; Etzelmüller et al., 2022; Rico et al., 2021; Legay et al., 2021). This approach has the advantage of reaching good performances while requiring only basic climatic input, i.e. air temperature and solar radiation.

An additional source of data used to complement modeling efforts in the context of rock wall permafrost is offered by the Electrical Resistivity Tomography (ERT). The ERT is a well-established method in rock wall permafrost research/investigations, which has been demonstrated to provide information about the electrical properties with high spatio-temporal resolution that can be interpreted in terms of the thermal state of subsurface materials (Hilbich et al., 2008; Keuschnig et al., 2017; Magnin et al., 2015b; Krautblatter et al., 2010; Scandroglio et al., 2021; Duvillard et al., 2021). ERT data can be acquired in complex terrain and gather relevant information in relatively short time (Magnin et al., 2015b;). The ERT data allow to observe frozen/unfrozen patterns in the bedrock, that can be compared to the numerical simulations of ground temperatures providing an additional source of model testing (Duvillard et al., 2020). In particular, this methodology develops a bidimensional transect of ground freezing conditions at a given survey date, which can validate 2D numerical simulations (Magnin et al., 2017; Etzelmüller et al., 2022).

The aim of this study is to move a first step towards understanding the distribution patterns and future evolution of rock wall permafrost in Greenland. To do so, we focus on the Sisimiut area, (68° N on the west coast). In fall 2020, we installed 9 surface

temperature loggers in the area measuring Rock Surface Temperature (RST), covering the local range of elevations and aspects. Using these data, we train a statistical model to evaluate the correlation between weather variables (i.e. air temperature and incoming shortwave solar radiation) and measured RST. Weather data belong to different sources and are downscaled using the TopoSCALE algorithm (Fiddes and Gruber, 2014). The statistical model is then used to compute the boundary conditions for a heat transfer model. In this study, we use COMSOL Multiphysics® heat transfer module (COMSOL Inc., 2015). We calibrate and test our model with temperature data obtained by two 100 m deep boreholes drilled in bedrock at low elevation in 2019 and 2021. To obtain field data on ground temperature in mountain terrain, we used the ERT approach proposed by Duvillard et al. (2020). We aim to answer three research questions:

1. Can our model reproduce permafrost patterns in agreement with our dataset?

2. What is the current distribution of rock wall permafrost in our study site?

3. What is the possible evolution of rock wall permafrost by the end of the 21st century under different RCP projections?

Overall, this study provides an insight on rock wall permafrost distribution in central-West Greenland, highlighting how this system is sensitive to recent and future climate variability.

2 Study site

Our study site is located in the mountains surrounding Sisimiut, a city on the coastline of the widest non-glaciated area in West Greenland, about 200 km from the Greenland Ice sheet (see Fig.1). Sisimiut is the second largest city in Greenland, counting 5582 inhabitants in 2020 and experiencing a rapid development. The city is surrounded by two main mountain ridges: the Nasaasaaq – Appillorsuaq ridge to the south, summiting at 784 m.a.s.l., and the Palasip Qaqqa– Sammisoq ridge to the north, summiting at 605 m.a.s.l. (see Fig. 1a). The landscape is characterized by narrow fjords, alpine summits and isolated coastal glaciers. The dominant lithology is amphibolitic gneiss (Ljungdahl, 1967). The mountains of the region typically have pyramid-shaped summits and steep rock walls generating debris slopes underneath. Mountains are dominated by bedrock, although vegetation patches are common at up to 400 m.a.s.l.

Sisimiut, located in the low arctic oceanic area, is subject to climate data collected at the airport weather station (Cappelen et al., 2021; Cappelen and Jensen, 2021) (see Fig. 1b). The climate in this region exhibits distinct characteristics. July, with an average temperature of 6.3 °C, marks the warmest month, while March is the coldest at -14.0 °C. These climatic characteristics classify Sisimiut within the sporadic permafrost zone (Obu et al., 2019; Biskaborn et al., 2019) and morphologically active rock glaciers extend to sea level elevation (see Fig. 1a).

The climate has undergone significant changes over the years. The mean annual Air Temperature (AT) increased from -3.5 °C during 1961-1981 to -1.8 °C in the period from 2000-2020. This shift in climate is also reflected in precipitation patterns. Mean annual precipitation decreased from 509 mm between 1961-1981 to 422 mm in 1984-2004, which coincides with the year the rain gauge was decommissioned. The reduction in precipitation affects both solid and liquid forms. For solid
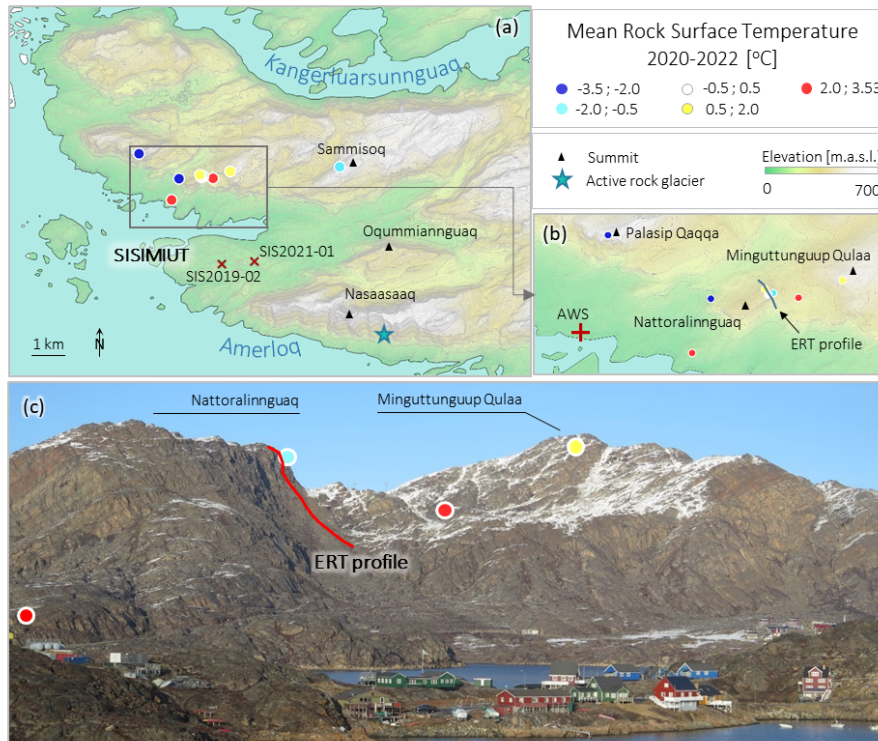
Figure 1. Study site summary. Map of the entire study area (a), with location of deep boreholes SIS2019-02 and SIS2021-01, main summits and active rockglacier. Detail of the Nattoralinnguaq area, where most of the RST sensors are installed (b). South face of Nattoralinnguaq and Miguttunguup Qulaa (picture taken from Sisimiut in October 2020) with RST loggers and geophysical profile locations (c). Loggers are colored based on their measured mean RST acquired during the acquisition period (fall 2020 to fall 2022). Elevation data belong to the Arctic DEM (Porter, 2018).

precipitation, mean monthly levels in January-April decreased from 28 mm in 1961-1981 to 25 mm in 1984-2004. Meanwhile, liquid precipitation, observed from June to September, dropped from 58 mm in 1961-1981 to 49 mm in 1984-2004. Recent

90   climate change is believed to be responsible for significant glacial retreat along the coast. Coastal glaciers in the area have lost approximately a quarter of their volume over the past three decades (Marcer et al., 2017).

3   Methods

3.1   Rock temperature monitoring

Rock temperatures are monitored by a network of temperature sensors installed in various settings across the study area. All

95   sensors used for the temperature data acquisition were custom zero-point calibrated using a Fluke 7320 compact bath with a manufacturer specified temperature stability and uniformity better than 0.01 °C. The bath temperature was measured using a

	RST		Deep Boreholes	
Nb	5	4	1	1
Brand	Geoprecision	Geoprecision	Geoprecision	HOBO
Type	MLog5W Rock	MLog5W STRING	MLog5W STRING	5-inch Probe
Sensor	PT1000	Tnode	Tnode	U12-015-02
Resolution [°C]	0.001	0.01	0.01	0.03
Accuracy [°C]	0.1	0.1	0.1	0.25
Logging interval [h]	1	1	1	0.00028
Sensor(s) depth [m]	0.3	0.3, 0.9	[0.1,0.5,1.0,1.5,2.0,3.0, 4.0,5.0,7.5,10.0,12.5,15.0, 17.5,20.0,25.0,30.0,35.0,40.0, 45.0,50.0,55.0,60.0,65.0,70.0, 75.0,80.0,90.0,99.0]	[1,5,10,15,20,25, 30,35,40,45,50,55, 60,65,70,75,80,85, 90,95,97.5]
Terrain	Steep bedrock	Steep bedrock	SIS2021-01	SIS2019-02

Table 1. Summary of the temperature sensors and their specifications used in the study area.

Fluke PRT 5610 secondary standard temperature probe, and each sensor was immersed in the bath for 40 minutes while logging every 30 seconds. After the sensor temperature stabilized, the sensor offset was calculated as $\Delta T = (\sum_{(i=1)}^{n}[T_{ref,i} - T_{s,i}])/n$, where $T_{s,i}$ [°C] is the ith sensor temperature measurement in the calibration period, $T_{ref,i}$ [°C] is the corresponding bath temperature measured by the PRT sensor at the same time, and ΔT [°C] is the average calculated sensor offset, which was applied as a correction to each field temperature measurement collected by that sensor.

We established a RST monitoring network consisting of 9 individual monitoring locations, covering as evenly as possible the range of aspects and elevations of the rock walls in the study site (see Fig. 1a). Data were acquired for two years, from fall 2020 to fall 2022. The technical information about loggers used are summarized in Table 1. Geoprecisions are widely used in permafrost studies and the community has previous experience in their strength and weaknesses (Gruber et al., 2004; Magnin et al., 2015a, 2019; Hipp et al., 2014; Duvillard et al., 2020). According to our calibration, Geoprecision offsets reach a maximum of 0.10 °C. Finally, Geoprecision loggers can be accessed remotely, allowing download of data within 10-20 m range, which becomes handy in steep terrain. The sensors were placed in 10 x 300 mm holes, thereafter sealed with frost resistant resin.

While deep boreholes in rock walls are not available in our study area, we have valuable data from two 100 m deep boreholes, SIS2019-02 and SIS2021-01, which were drilled in bedrock outcrops on flat terrain at 50 and 70 m.a.s.l. (see Fig.1a). While these locations differ from our primary focus on rock wall permafrost, we have incorporated their data into this study and will address the associated limitations in our discussion. The boreholes are located in similar conditions regarding the exposure to

solar radiation, yet different snow conditions. SIS2019-01 is located in a drift accumulation area and the snow depth can reach
115 2 m, while SIS2021-01 is on a wind-exposed hill, which ensures snow-free conditions most of the winter. Both boreholes are
drilled using a Sandvik DE130 compact core drill owned and operated by the Greenland School of Minerals and Petroleum,
with wireline NQ drilling tools (outer diameter: 70 mm). The holes are installed with a 100 m long PE casing (outer diameter
32 mm, inner diameter 26 mm), closed at the bottom with a heavy duty heat shrink end cap with heat activated glue.

Borehole SIS2019-02 does not have a permanent sensor installed, and the available dataset consists of four temperature
120 profiles logged manually. This was done at three distinct dates: 27 October 2020, 17 November 2020, 20 January 2021 and 9
November 2021. For each measure we use a HOBO U12-015-02, logging at 10 s sampling interval and resting at predefined
depths for two minutes (see Table 1 for measuring depths). In the post processing, temperatures are averaged only over the
last minute to obtain the temperature at a particular depth, thereby ensuring the sensor has equilibrated to the new temperature.
The borehole SIS2021-01 is equipped with a permanent GeoPrecision thermistor string with 28 sensors (TNode, digital chip
125 with 0.01 °C resolution). The upper-most sensor is located at 0.1 m.b.g.s., the lower-most at 99 m.b.g.s. The sensor spacing
progressively increases with depth from 0.4 m in the top to 10.0 m at depth, and the logging interval is 1 hr.

3.2 Geophysical data

To obtain information on deep permafrost distribution in mountain terrain, we use the approach proposed by (Duvillard et al.,
2020), consisting in a combination of ERT measurement on the field and laboratory experience to calibrate the temperature-
130 resistivity relationship characteristic of the rock. The ERT measure takes place in October 2020, across the north and south
faces of Nattoralinnguaq (353 m.a.s.l) (see Fig. 1b). This summit presents typical characteristics of the mountains in the Palasip
Qaqqa– Sammisoq ridge: a steep and rocky south face approximately 100 m high with a debris slope underneath, and a more
gentle north face characterized by small vegetation patches and some short steeper sections (see Fig. 1c).

The ERT measure consists of one profile 450 m long (five 100 m long cables and a total of 100 electrodes deployed with 5
135 m spacing). We use a 12 V external battery for powering the resistivity meter (Guideline Geo Terrameter LS2) and injecting
the current. We use 10 mm x 100 mm stainless steel electrodes, inserted in pre-drilled holes with a paste of salty bentonite
to improve the galvanic contact/reduce the contact resistances and prevent freezing (Krautblatter and Hauck, 2007; Magnin
et al., 2015b). For the data collection, we use the Wenner configuration because of its best signal-to-noise ratio in complex
environments (Dahlin and Zhou, 2004; Kneisel, 2006). Topography was extracted from a 2 m resolution digital elevation
140 model (DEM, Porter (2018)) based on electrode positions measured with a handheld GPS device. We cleaned 4% of the
measures acquired before the inversion (549 measures acquired, 528 inverted) by filtering out the outliers from the pseudo
section. The data were inverted with the RES2DINV-4.8.10 software using a smoothness-constrained least-squares method
and the standard Gauss–Newton method (Loke and Barker, 1996). The inversion was stopped at the third iteration when the
convergence criterion was reached, i.e. when the RMSE variation versus the previous iteration is below 10%.
145 In addition to the field measurements, we perform a laboratory electrical conductivity experiment on three rock samples
following the procedure described by Coperey et al. (2019). These analyses define the relation between resistivity collected
in the field and rock temperature, under the assumption that the material is not fractured and isotropic. The rock samples are

collected from the rock walls on the south and north face (sample G-RF, G-LR and G-DA) and are characterized by a porosity of $\Phi = 0.032$ for G-RF, $\Phi = 0.015$ for G-LR and $\Phi = 0.023$ for G-DA. Before performing the laboratory measurements, each sample is cut in a 4 x 4 x 4 cm cube, is dried for 24 hours at 60 °C, and eventually saturated under vacuum with degassed water from melted snow taken in the field. The cubes are then left several weeks in the solution to reach chemical equilibrium. The water conductivity at 25 °C and at equilibrium is 0.0118 S m^{-1} for G-DA and 0.0142 S m^{-1} for G-RF and G-LR. The cubes are then placed in a heat-resistant insulating bag immersed in a thermostat bath (KISS K6 from Huber; bath volume: 4.5 l). The bath temperature is regulated using an internal sensor with a precision of 0.1 °C, while the rock temperature is monitored with an additional sensor, also offering a precision of 0.1 °C. Glycol is used as heat carrying fluid and the conductivity measurements are carried out with the impedancemeter. The glycol is progressively cooled from 20 °C to -13 °C, stopping for 2.5 h at predefined temperatures to let the rock reach thermal equilibrium with the glycol. After the equilibrium is reached, the resistivity is measured.

3.3 Modeling

Our modeling approach is based on a mixed statistical-numerical methodology, which is conceptually similar to the study developed by Magnin et al. (2017). The methodology evaluates RST time series with an empirical approach, which are then used as upper boundary conditions for a heat transfer numerical model. This modelling methodology refers to a four-steps workflow: (i) acquisition of weather forcing data and downscaling, (ii) statistical modeling and prediction of RST data, (iii) numerical modeling of heat transfer in bedrock, and (iv) model validation with field data.

3.3.1 Weather data and downscaling

The weather data are retrieved form different sources covering different periods - summarized in Table 2. Our time domain is divided in three periods: (i) the historical period from 1870 to 1969, (ii) the current period from 1970 to 2022, and (iii) the future scenarios from 2023 to 2100. While a weather station at the Sisimiut airport has been recording AT since 1961 (Cappelen and Jensen, 2021) (dataset d in in Table 2), it is noteworthy that such long-term data collection is rare in most areas in Greenland. Consequently, we have chosen to utilize weather data available at the regional scale to force our model, and keep the Sisimiut weather station data as validation set. This choice allows us to understand the modeling uncertainties inherent in regional-scale weather data, with the broader aim to assess how this methodology could be applied in other areas of the region. Therefore, we evaluate the performance of each of the following dataset by comparing their AT to the data from the Sisimiut weather station over the overlapping period.

The weather data for the current period are obtained from the ERA5 reanalysis, that we downloaded from the Copernicus database (Hersbach et al., 2020) (dataset b in in Table 2). For this study, we use the AT at pressure levels from 1000 hPa to 500 hPa and Shortwave Solar Radiation Downwards (SSRD) at the surface level.The time series are downscaled using the TopoSCALE algorithm (Fiddes and Gruber, 2014). TopoSCALE models surface AT by interpolating the AT profile at the different pressure levels. SSRD is donwscaled by evaluating the topographical shading effect on the SSRD. The elevation data are obtained from the Arctic DEM at 10 m resolution (Porter, 2018). In order to optimize the computation time, we use the

Dataset reference	Label	Period Available	Period used	Variables	Data type	Location
Custom made	a	1784-2021	1870-1959	Air temperature Solar radiation	Interpolation from e1, e2* and b Extrapolated from dataset b	Sisimiut
Herbasch et al 2019	b	1970-present	1970-2022	Air temperature, solar radiation	Reanalysis	Global 0.5 degs
Bentsen et al, 2013, RCP 2.6	c	2006-2100	2023-2100	Air temperature, solar radiation	CMIP model	Global 2 degs
Bentsen et al, 2013, RCP 8.5	d	2006-2100	2023-2100	Air temperature, solar radiation	CMIP model	Global 2 degs
*Used to generate air temperature of dataset a						
Cappelen et 2021a	e1	1784-2021		Air temperature	Weather station	Nuuk
Cappelen et 2021a	e2	1784-2021		Air temperature	Weather station	Ilulissat
Validation Dataset						
Cappelen et 2021b	d	1961-2021		Air temperature	Weather station	Sisimiut

Table 2. Summary of the weather databases used to cover the investigation period (1870 -2100). Dataset a is used to describe historical weather. Dataset b is used to describe current weather. Datasets c and d are used for simulating scenarios RCP 2.6 and RCP 8.5 respectively. Datasets e1, e2, and b are used to model AT in Sisimiut for dataset a. Dataset d is used as AT validation data. Dataset b is used to calibrate the RST model (See Sect. 3.3.2). Datasets a, b, c, and d are used to force the heat transfer simulations (See Sect. 3.3.3)

TopoSUB algorithm to optimize the computation of the terrain parameters in the complex topography of our study site (Fiddes and Gruber, 2012).

The AT data for the historical period are computed using AT recorded in Nuuk (300 km south) and Ilulissat (250 km north) (Cappelen et al., 2021)(datasets e1 and e2 in in Table 2). To downscale the data, we compute the regression between these time series and the downscaled ERA5 time series over the overlapping period (1970 to 2022). The regression is then used to generate AT for the period 1870 - 1969. For SSRD, weather stations in Nuuk, Ilulissat and Sisimiut do not have this variable measured. For this dataset, we generated a synthetic SSRD estimation, equal to the average year over the period 1970-2022 retrieved from the downscaled ERA5 dataset.

For future scenarios, we use the Norwegian Earth System Model version 1 (NorESM1) global circulation model, using Representative Concentration Pathway (RCP) 2.6, and RCP 8.5 for 2006-2100 (Bentsen et al., 2013). The NorESM1 model is developed to focus on polar climate and is chosen by other authors in Greenland for cryosphere evolution modelling due to its good performance in the region (Colgan et al., 2016). The RCP 2.6 is the NoreESM1 outcomes for scenarios of declining emissions since 2020 (optimistic scenario, dataset c in Table 2), while the RCP 8.5 is simulated with unregulated emissions increasing at a rate compatible to the present-day industrial development (pessimistic scenario, dataset d in Table 2). To downscale the data, we compute the regression between these time series and the downscaled ERA5 time series over the overlapping period (2006 to 2022).

3.3.2 RST Modeling

In this step, we model the relationship between downscaled weather data and RST data using a conceptually identical approach to Magnin et al. (2019). The RST is predicted by an empirical model trained using available forcing variables that dominate

RST distribution on steep rock walls, i.e. AT and SSRD. To do so, we aggregate each RST measurement to the forcing data that occurred during that acquisition time step. RST data from the period 2020-2022 aggregated at monthly time steps are used as dependent variable. As predictors, we use AT and SSRD from the ERA5 dataset donwscaled at the respective logger location. This creates a database of Nx1 targets and Nx2 data points, where N is the number of available RST data.

The RST is modelled using a multinomial linear regression, trained with the Matlab function fitlm. To evaluate the validation performance, we follow the classic cross validation approach that iteratively splits the dataset randomly in 80% training and 20% validation, until all datapoints are used both as training and validation. To evaluate the test performance, we predict the RST time series at the borehole SIS2021-01 location and compare it to the data measured at 0.1 m depth, which is not used for the training/validation routine.

3.3.3 Heat transfer model

To describe deep rock temperatures, we develop a 1D numerical model that we calibrate with SIS2021-01 borehole data. The heat transfer is modelled using the "heat transfer in porous media" module in COMSOL, which assumes the local thermal equilibrium hypothesis to be valid and simulates conduction only. The model geometry consists in a 100 m 1D model. The model accounts for three materials: solid matrix, fluid and solid with phase change. The fluid phase is the default COMSOL "water" material, to which we assigned a phase change to ice at 273.15 K and transition interval to ice of 2 K, according to Noetzli and Gruber (2009). The matrix density is assigned in agreement to the data from the core extracted form SIS2021-01. The data show an increase from 2600 kg m^{-3} to 3000 kg m^{-3} at 20 m.b.g.s., and then remaining constant thereafter.

Since we do not have precise information on the rock thermal properties, we calibrate the specific heat capacity, thermal conductivity and matrix porosity of the solid phase. The calibration is carried out by simulating conditions in SIS2021-01, from 1870 to 2022 using a 1D geometry of a 100 m column. The simulation results are then compared to the field data acquired during the period August 2021 to April 2022. This is repeated for different combinations of thermal properties, targeting the minimization of the RMSE between the measured and modelled temperatures across the borehole depth.

The numerical simulation consists of three successive studies: a stationary study for initial conditions (mean conditions for 1870-1890, forcing dataset a), a transient study 1870-1969 (forcing dataset a) and a transient study 1970-2022 (forcing dataset b). All weather datasets are downscaled at the desired location using the TopoSCALE algotrithm, as described in Sect. 3.3.1. The corresponding RST time series is computed using the RST model developed in Sect. 3.3.2 and used as surface boundary condition.

As lower boundary condition, we impose the constant geothermal heat flux, which we evaluated from the temperature gradient of 0.015 °C m^{-1} measured from 100 to 90 m.b.g.s. at SIS2021-01. As initial conditions, we compute the temperature profile of the stationary solution of the 1D model forced by the average RST over the period 1870 - 1890. We then add a positive ground temperature offset as parameter to account the fact that temperatures in 1870 - 1890 (at the Little Ice Age peak) were lower than the previous period, and deep ground temperatures were likely higher than modelled by our stationary model. This temperature offset is also matter of calibration.

3.3.4 Model testing

To test the performance of the numerical model, we simulate rock temperatures using the calibrated thermal characteristics
and RST boundary conditions downscaled at the SIS2019-02 and the ERT profile locations. The former simulation is set up
using the 1D geometry described in the previous section. The latter simulation is set-up using a 2D geometry along a north-
south transect extracted from the DEM using QGIS (Quantum GIS, (QGIS, 2023)). The elevation profile is then imported into
COMSOL as 2D geometry using the parametric function option. We then evaluate the RST forcing indepedently at each profile
node using the approach described in Sect. 3.3.2. The RST time series are then parameterised as function of the spatial variable
(x) and temporal variable (t), and used as surface boundary condition for the 2D model. As lower boundary condition, we
impose the geothermal heat flux evaluated from the borehole SIS2021-01, while we impose zero-flux conditions on the lateral
boundaries.

3.4 Permafrost distribution and evolution

In this last section, we explore the present and future distribution of rock wall permafrost in the study area using the modeling
tools we have developed in the previous steps. At first, we use the RST model to compute rock wall temperature maps. This
allow us to visualize the potential distribution of rock wall permafrost. To do so, we first define the rock walls from the DEM
as terrain steeper than 40 degrees (Magnin et al., 2019). In the study site, 9.32 km^2 are steeper than $40°$ and classified as rock
walls. For each grid cell that qualifies as rock wall, we then compute the RST time series by predicting the RST model on the
donwscaled AT and SSRD time series for both the current period and the future scenarios. The rock wall temperature maps
are then computed by evaluating the Mean RST (MRST) for the period 2002-2022 and for the period 2080-2100 using both
scenarios RCP 2.6 and RCP 8.5.

In our second analysis, we focus on predicting the future evolution of deep rock temperatures at the SIS2021-01 location.
Given that our numerical model is calibrated to fit the data collected at this very site, the level of uncertainty here is arguably
at its minimum. To do so, we append a two independent transient studies to the heat transfer model generated in Sect. 3.3.3. As
upper boundary condition, we use downscaled RST time series for the two climate scenarios (RCP 2.6 and RCP 8.5, datasets
c and d in Table 2) from 2023 until 2100. We then compare the generated temperature profiles for 2100 and describe the
permafrost evolution at this site.

In our last analysis, we assess the evolution of mountain permafrost in complex terrain using a 2D modeling approach. Our
investigation centers on two specific locations: the ERT transect and the Nasaasaq summit ridge. The latter site is chosen to
observe the expected evolution of rock wall permafrost at the highest elevations in the area. For both locations, we employ 2D
models driven by RST time series from 1870 to 2100, which have been downscaled along the elevation profiles following the
methodology outlined in Sect. 3.3.4. We conduct the heat transfer model simulations for both RCP scenarios, allowing us to
compare their different impacts on rock wall permafrost

4 Results and Discussion

4.1 Rock temperature monitoring

RST data are measured during two full years, as loggers were installed in September - October 2020 and data collected in September - October 2022. Most loggers show sub-zero RST between early October and late May. Lowest RSTs are reached in late March, when several loggers recorded temperatures around -20 °C (see Fig. 2a). The lowest RST (-21.2 °C) is recorded on 25 February 2022 by a logger installed on a north facing bedrock slope at 314 m.a.s.l.. Highest RSTs are reached at the end July, as several loggers recorded temperatures above 25 °C. The data show that MRST is correlated with elevation and mean SSRD (see Fig. 2b). To show the effect of elevation, we compare two loggers installed on south facing rockwalls, one at 52 m.a.s.l. (MRST = +3.2 °C) and at 522 m.a.s.l. (MRST = +0.6 °C), giving a MRST gradient of 0.0055 °C m^{-1}. By comparing loggers installed on rock walls at the same elevation but on opposite aspects, we obtain a MARST offset of 2.2 °C from north to south facing slopes.

Boreholes temperatures are shown in Fig. 2b and Fig. 2c. SIS2021-01 (see Fig. 2c) shows consistently negative temperatures between 20 and 70 m depth, reaching a minimum of -0.2 °C at 30 m depth. The depth of zero annual amplitude is approximately 10 m.b.g.s.. Since we measure negative temperatures below this depth, the data from SIS2021-01 indicate the presence of permafrost. In SIS2019-02 (see Fig. 2d), temperature data indicate a minimum of temperature of +0.3 °C, reached at 30 m depth, and a temperature of +1.0 °C at 100 m. The depth of zero annual amplitude is approximately 20 m. Since temperatures are positive below the depth of zero annual amplitude, the measurements at SIS2019-02 indicate absence of permafrost.

In comparing the contrasting conditions between SIS2019-02 and SIS2021-01, it is important to note that SIS2019-02, situated at the same elevation and in a slightly more shaded location than SIS2021-01, exhibited lower solar radiation levels (90 Wm^{-2} versus 104 Wm^{-2}) during the period 1970-2022. Given this difference, one might anticipate that SIS2019-02 would display permafrost conditions, as observed in SIS2021-01. We propose that the temperature data indicate that the presence or absence of permafrost is influenced by the distinct snow cover characteristics at these two sites. In arctic climates, snow drifts often form early in the season, and these drift patches persist across different seasons (Parr et al., 2020). The early onset of snow cover has a warming effect on the ground, and when this pattern recurs each winter, as is suspected to occur in SIS2019-02, it can result in a warmer ground compared to a wind-exposed area such as SIS2021-01.

Overall, the temperature data delineate discontinuous permafrost conditions in rock walls and bedrock. Given the range of elevation where permafrost is found, this conditions are similar to those described in Northern Norway (69 – 71° N), where negative MRST and rock wall permafrost can be found at sea level on north facing slopes (Magnin et al., 2019). This offset is known to be dependent on latitude, varying from 8 °C in the European Alps (45-46° N, Magnin et al. (2015a)) to 1.5 °C in Northern Norway (69-71° N, Magnin et al. (2019)). In coastal climates, previous studies suggested that steep bedrock permafrost could be influenced by other factors than pure solar radiation, as cloudiness and icing, creating an abnormally low offset in New Zealand (Allen et al., 2009). Despite the fact that the Sisimiut mountain area is coastal, our data suggest that this process is not a relevant factor for rock wall distribution in the area.
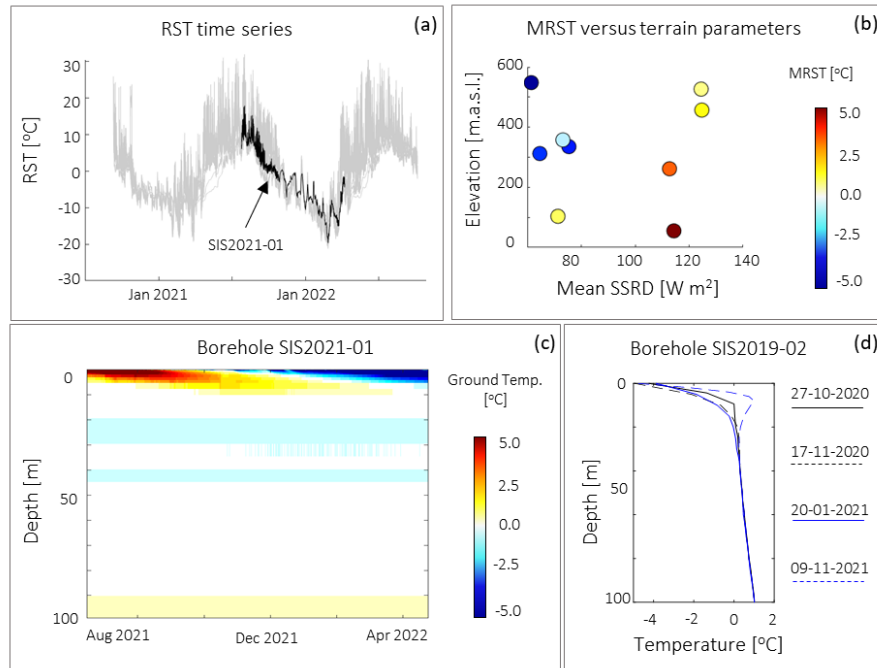
Figure 2. Summary of temperature recorded by the loggers during 2020-2022. RST time series for all loggers (a). In black, is shown the RST recorded at SIS2021-01; this dataset is used as test set for the RST model (See Sect. 3.3.2). Relationship between MRST recorded during the observational period (2020-2021) in relation to topographical predictor Elevation and mean SSRD during the observational period (b). Temperature data from boreholes SIS2021-01 (c) and SIS2019-02 (d). For borehole SIS2021-01, data are acquired with an interval of 1 hr using a MLog5W-STRING, allowing us to color plot temperatures as function of depth and time. For borehole SIS2019-02, data were measured on four separate dates, using a 5-inch Probe lowered manually into the borehole. These measurements produce four temperature profiles, i.e. temperature as function of depth,

4.2 Geophysical survey

As shown in Fig.3a, the conductivity values measured along the profile vary from values below 10^{-2} Sm^{-1} up to 10^{-6} Sm^{-1}. According to the petrophysical analysis, shown in Fig.3b, this range of conductivity highlights the co-existence of frozen and
300   unfrozen conditions. Although the precise relationship temperature - conductivity is dependent upon the single sample, the analysis shows a common pattern of sharp increase in conductivity as soon as 0 °C temperature is reached. This feature occurs between $10^{-4.4}$ and $10^{-3.5}$ Sm^{-1} for all samples. Therefore, this range of conductivity values is used as thresholds to define frozen, unfrozen and transition zones in the ERT tomogram. In the transition zone, our analysis is not able to discern between frozen and unfrozen conditions.
305   When applying these thresholds to the ERT field data, we can describe the patterns of frozen and unfrozen conditions of the mountain (See Fig.3a). Frozen conditions occur in the central section of the north face, at 300 - 350 m.a.s.l.. The frozen
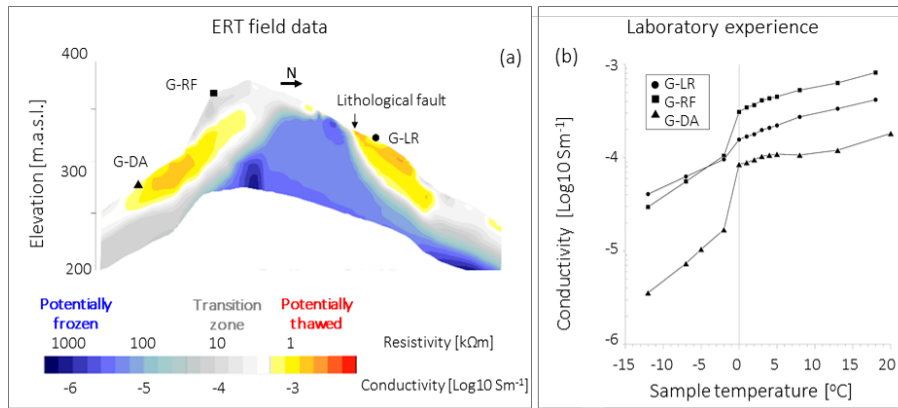
Figure 3. Summary of the geophysical survey. Profile of electrical conductivity/resistivity tomography (in Sm^{-1} and $k\Omega m$) measured on the field (a). Petrophysical analysis, showing electrical conductivity data versus temperature for the three samples collected along the geophysical profile (b).

area reaches depths well below the depth of zero annual amplitude, indicating the presence of permafrost at this location. The summit and most of the south face are in transitioning conditions, indicating warmer temperatures than the central section of the north face. The south face is also characterized by a large unfrozen body, which we interpret as absence of permafrost in 310 the rock wall.

Unfrozen conditions are also shown on the lower section of the north face, below 300 m.a.s.l.. The presence of unfrozen conditions at this location is in contrast with our understanding of permafrost distribution in the area. Permafrost is expected to exist on north facing steep terrain already at low elevation, as highlighted by RST and borehole data described in the previous section. Additionally, since this location is characterised by north facing aspect and higher elevation compared to SIS2021-01, 315 we would expect colder conditions than the data collected from the borehole. Although snow may play a warming role as observed in SIS2019-01, this section of the face has slopes that guarantee snow free conditions thorough the winter. To explain this anomaly, we highlight that this area coincide with a large lithological fault observable on the field. As result, the ERT tomogram shows a sharp transition in conductivity values. We suggest that the ERT data at this location are strongly influenced by other factors than bedrock temperature, such as weathering and dense fracturing. These factors challenge the isotrophic 320 conditions that are necessary to meaningfully compare laboratory analyses to the ERT tomogram. All considered, we consider the ERT data at this location to be unreliable and we disregard this area of the tomogram in our further analyses.

Overall, the geophysical survey indicate that, at this location, permafrost is discontinuous. Up to this elevation (400 m.a.s.l.), the data describe either frozen or unfrozen conditions depending upon we are on a north or south facing rock wall respectively. This observation is in agreement with the RST data described in the previous section. The co-existence of frozen, unfrozen and 325 transitioning conditions suggest that deep permafrost has temperatures close to thawing point. This is in agreement with the borehole data described in the previous section.
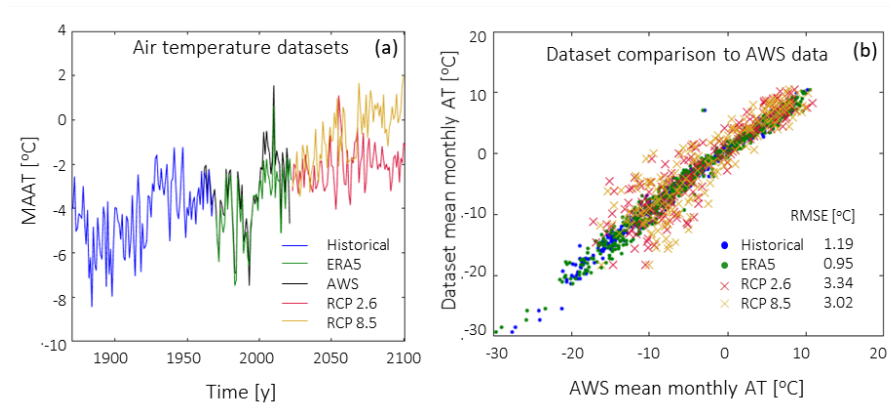
Figure 4. Weather data summary. Yearly time series of the different AT datasets, downscaled at the weather station location (a). Ccomparison between AWS AT and donwscaled datasets AT during the overlapping periods (b).

4.3 Modeling

4.3.1 Weather data and downscaling

A sample time series of the available weather data is shown in Fig.4a, while the validation scatterplots of the AT data are
330 shown in Fig.4b. The validation indicate a RMSE of 0.95 °C between the AWS AT data and the ERA5 AT donwscaled at the weather station location. This value is comparable to previous studies using this dataset in Greenland (Delhasse et al., 2020) and in complex terrain when downscaled with TopoSCALE (Fiddes and Gruber, 2014). The historical database has a similar performance, showing a RMSE of 1.28 °C.

The data from the NorESM1 scenarios have higher RMSE, indicating a poorer fit between the data and model. We believe
335 this is an intrinsic characteristic of the model, as the mean errors between measured and modeled AT is consistent with the average error over continents declared by Bentsen et al. (2013), i.e. -1.09 °C. This indicates that the dataset, when compared to historical data, tends to underestimate land temperatures.

It is important to notice that this analysis quantifies the performance of the AT data at sea level. Since our study evolves in complex terrain, a comprehensive evaluation of the weather database requires weather data at different elevations and including
340 SSRD. Since we do not posses such data, we refer to the work from Fiddes and Gruber (2014) indicating that the TopoSCALE algorithm provides consistent performance across complex terrain. This suggest that we should expect similar data quality at different elevations and aspects. However, a detailed description of this source of uncertainty remains missing at this location.

4.3.2 RST Model

The training, validation and test results of the RST model are summarized in Fig.5. The model has consistent performance
345 in training, validation and test, described by a stable RMSE ranging from 1.99 °C to 1.96 °C. To better contextualize this
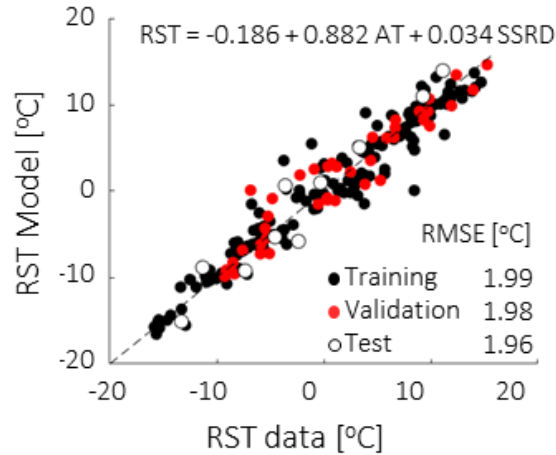
Figure 5. Summary of the RST model. The model is a function of AT and SSRD. Data are aggregated at monthly time step. Training and validation data are acquired to the RST loggers. Test data are acquired by SIS2021-01.

performance, we compare our model to Schmidt et al. (2021) which represents the state of the art of RST modeling in the arctic. Their approach is based on the SEB module of CryoGrid 3, modified to account for vertical terrain, including vertical moisture transport affected by latent heat flux and skyview factor adapted to steep terrain. By comparing model runs and field data, Schmidt et al. (2021) obtained R^2 above 0.97 and RMSE below 1.20 °C on monthly RST data. This value indicates a
350 better performance than our model. This is likely due to their use of a more sophisticated model, as well as in-situ weather station data as forcing AT. For sake of comparison, if we force our model with AT from the local AWS, we obtain a lower RMSE, i.e. 1.46 °C, indicating that part of our RMSE is due to the uncertainty of the weather forcing. While it is possible in principle to utilize weather station data to drive our model and enhance its performance, our preference is to evaluate the model performance and associated uncertainties using regionally available data.

355 **4.3.3 Heat transfer model**

The results of the heat transfer model calibration and validation are summarized in Fig.6. The calibration of the heat transfer model indicated that the model is mostly sensitive to the porosity value, in agreement to Noetzli and Gruber (2009). According to their study, porosity dominates the sensitivity on short time scales (e.g. decades), while the matrix thermal parameters dominate the sensitivity on longer time scales (e.g. millennia). The calibration yielded an optimal porosity value of 1.5%, while the
360 optimal initial offset was determined to be +0.8 °C relative to the MRST during the period 1870-1890. The thermal parameters were initially set to the default crystalline rock matrix in COMSOL: K = 2.9 $Wm^{-1}K^{-1}$ and Cp = 850 $Jkg^{-1}K^{-1}$. These initial values provided the minimal difference between model run (Fig.6a) and SIS2021-01 data (Fig.6b) that we managed to achieve. Consequently, we maintain these parameters unaltered form their default settings.

To visualize the model performance, we plot the RMSE distribution between model and data across the borehole depth, as showed in figure Fig.6c. The maximum RMSE is measured at 1 m depth (4.02 °C), while it drops consistently below 0.20 °C below 10 m.b.g.s.. When evaluating the RMSE over the entire measurement period, we observed values ranging from maximum of 0.70 °C at surface, to below 0.10 °C below 10 m.b.g.s., to below 0.01 °C below 80 m.b.g.s. (Fig.6c). To contextualize the model performance, we compare our results to Magnin et al. (2017), who use a similar trainsient modeling approach. It must be taken into account that a direct comparison is difficult as, in our case boreholes are on flat terrain, while Magnin et al. (2017) have data from boreholes drilled on vertical bedrock, arguably less influenced by lateral variability in ground characteristics and snow cover. Given this, Magnin et al. (2017) also observes large discrepancies between model and data from the rock surface down to 6 m depth. At 10 m depth, their model has performances varying from 0.70 °C to 0.01 °C, depending on the borehole and time aggregation used. This indicates that our RMSE is comparable with their findings, further proving that this modeling approach is valuable for predicting rock temperatures where heat transfer is dominated by conduction. At shallower depths, advective heat transfer, due to water and air circulation in cracks, drives temperature patterns that can not be modelled by this approach. Although recent studies are developing numerical approaches to quantify these effects (Magnin et al., 2020), it is not currently possible to apply such methods beyond the site scale.

4.3.4   Model testing

When tested and compared to SIS2019-02 (Fig.6d), the model shows the same error pattern decreasing with depth observed for SIS2021-01, indicating discrepancies up to 2 °C above the depth of zero annual amplitude (20 m depth). Considering that all temperature profiles at this location were recorded in fall - early winter, it seems that the model over-estimates shallow rock temperatures during this period. These cold anomalies in the measured data could be due to advective heat transfer processes in the rock cracks, possibly enhanced by the flat terrain, e.g. cold rain infiltration.

Concerning the temperatures below the depth of zero annual amplitude, the model shows a cold bias, with values 0.85 °C to 0.75 °C lower than the data. We believe this effect is due to the fact that this borehole is located in an area of recurrent snow drift accumulation, as explained in Sect. 4.1. In particular, our model does not take into account snow accumulation and it represents ground temperatures in an hypothetical snow-free location with the same AT and SSRD as in SIS2019-02. The difference between our model and the borehole data suggests that recurrent snow cover has a warming effect on deep ground temperatures, which the analysis indicates to be of 0.80 °C. Considering this effect, summed to the model RMSE distribution described in the previous section, our model results can deviate -1.0°C to 0.2°C from the data below 10 m.b.g.s.. When snow cover exists, our model is colder than the actual deep rock temperatures, reason why this temperature interval is skewed towards the negative temperatures. This temperature range describes our uncertainty range when predicting rock permafrost conditions in areas where snow may or may not accumulate, i.e. generic bedrock terrain. In the following analysis we will refer to this uncertainty range as *transition zone*. Similarly to the transition zone described for the ERT tomogram in Sect. 4.2, here our heat transfer model results are uncertain in discerning frozen form unfrozen ground conditions.

As additional model test, we present the 2D model simulation at the geophysical profile location (Fig.7). According to the numerical model output, 55 % of the ERT transect area shows frozen ground conditions, while 2 % is expected to be in unfrozen
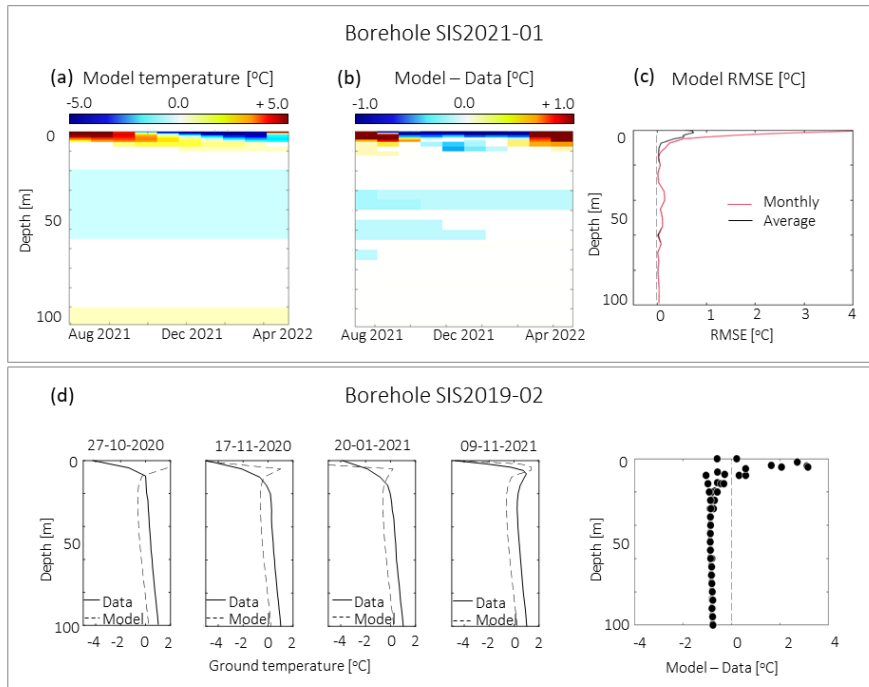
Figure 6. Summary of the heat transfer model calibration and testing with borehole data. All plots are issued by the model calibrated with the parameter values described in Sect. 4.3.3. Heat transfer model run for the observational period of SIS2021-01 (a). Difference between measured temperatures and model results at SIS2021-01 (b). RMSE between model and observations, aggregated at monthly time steps and over the entire observational period (c). Comparison between profile temperatures at SIS2019-01 and summary of model errors in function of borehole depth (d).

conditions. 43 % of the transect is within the transition zone, i.e. the numerical model predicts a rock temperature within -1.0 °C and 0.2 °C and the model is uncertain in assigning either frozen or unfrozen conditions within this range. Similar values are
400 provided by the ERT tomogram (48 % frozen, 37 % transition and 15% unfrozen). Overall, the model and the ERT tomogram have a 74 % agreement, although the model predicts generally colder conditions than the ERT tomogram. It is unclear whether it is our numerical model to overestimate permafrost extents, or conversely the ERT tomogram to underestimate permafrost extents.

In particular, the model shows the lower section of the south face of the mountain to be permafrost free, with ground
405 temperatures above zero at 10-20 m depth. Below the summit and towards the south face side of the mountain, temperatures are in the range of 0.5 to -1 °C, indicating a transition zone between frozen and unfrozen ground. This pattern of warm south face with transitioning conditions from frozen to unfrozen is in agreement with the ERT tomogram, although the latter method shows a larger unfrozen area. The numerical simulation predicts negative temperatures across the whole north face. This pattern is confirmed by the ERT tomogram, which shows frozen conditions on the upper part of the face, albeit being the unfrozen
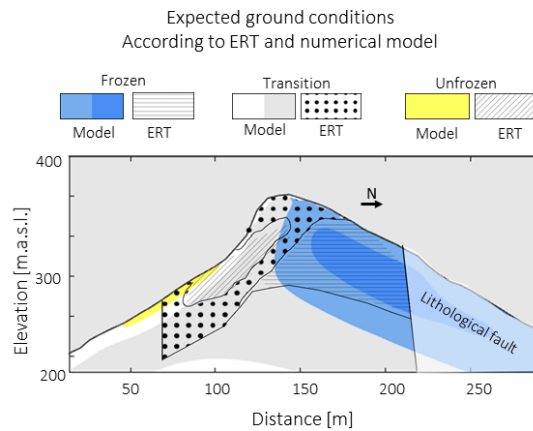
Figure 7. Comparison between the 2D heat transfer model run at the ERT transect location and the ERT data. Ground is described with respect to its conditions, varying from frozen and unfrozen. Transitional conditions indicate the uncertainty range of the two methodologies in discerning frozen from unfrozen ground conditions. The colors indicate ground conditions as described by the heat transfer model, while patterned areas indicate ground conditions as described by the ERT tomogram.

area expected to be smaller. As explained in Sect. 4.2, the lower section of the north face is characterized by the presence of a lithological fault affecting the ERT tomogram, and any comparison with the numerical simulation is meaningless here.

Overall, the two models show agreeing patterns of permafrost distribution, as they both indicate discontinuous permafrost across the mountain and a dominance of the SSRD in discerning between frozen and unfrozen conditions. We consider the 74% agreement between the two methods as satisfactory, as it is sufficient for us to confirm the main permafrost patterns at this location.

4.4 Permafrost distribution and expected evolution

According to our RST model, during the period 2002-2022, 63% of the rock walls (i.e. 5.85 km^2) have negative MRST and likely host permafrost, as summarized in the polar plot in Fig.8a. North facing rock walls can reach negative MRST already at sea level, while south facing rock walls are likely to host permafrost starting at 500 m.a.s.l.. The colder MRST occurs on the north faces of the Nasaasaaq peak (763 m.a.s.l.), reaching -3.0 °C. For the RCP 2.6 (Fig.8b), in 2080-2100 is simulated an increase in elevation of the MRST 0 °C isotherm of 150 m. This causes a 9% loss of rock wall permafrost extents, from 5.85 km^2 to 5.31 km^2. For the scenario RCP 8.5 the impact on permafrost is severe (Fig.8c), as, in the period 2080-2100, permanently frozen ground disappears from most of the study area, except for the north faces of the highest summits covering 0.08 km^2 (less than 1% of the rock walls in the study area).

While the MRST maps show the impacts of future climate change on the surface, numerical simulations quantify the ground temperatures below the surface. The simulations conducted at SIS2021-01 show that, regardless the scenario used, permafrost
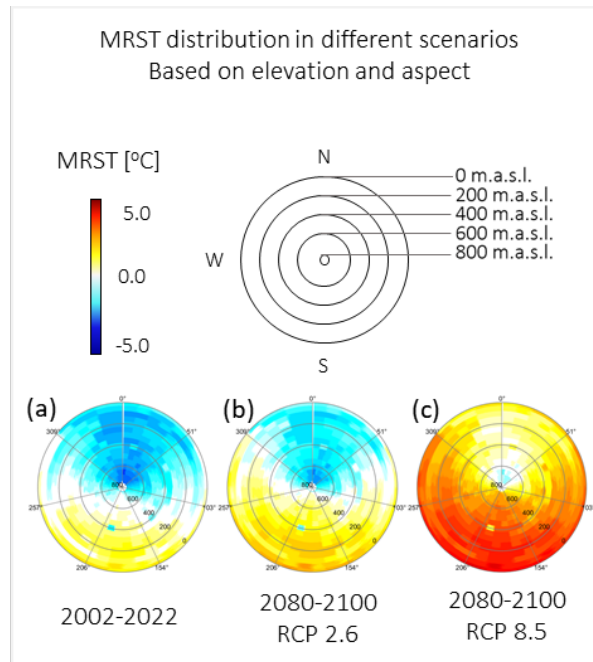
Figure 8. Summary of rock wall MRST distribution at different times and scenarios. The summary are presented as polar plots, where the color-coded MRST is presented as a function of aspect and elevation. RST distribution is averaged over the periods 2002-2022 (a) and 2080-2010 for scenarios RCP 2.6 (b) and RCP 8.5 (c).

conditions will disappear by the end of the 21st century (Fig.9a). For scenario RCP 2.6, the lowest ground temperature is modeled at 60 m.b.g.s., reaching 0.07 °C (Fig.9b). For scenario RCP 8.5 ground temperatures are consistently above 0.22 °C (Fig.9b). In 2100, ground temperatures at 20-50 m depth are about 1 to 1.5 °C higher for the RCP 8.5 compared to RCP 2.6,
430   indicating that, due to thermal inertia of the ground, surface heat is not yet fully propagated at depth by 2100 in this scenario.

A similar result is obtained when evaluating the expected ground temperature evolution in complex terrain by the 2D model (Fig.10). For the ERT location (Fig.10a), the model forced with the scenario RCP 2.6 suggests an increase of the temperatures of the permafrost body of 0.7 °C, causing minimum ground temperatures to be within our model transition zone. This indicates that, at this location, permafrost is expected to exist at temperatures close to thawing point and only underneath extensive snow
435   free areas. Scenario RCP 8.5 delineates a situation where transitioning conditions still exist, but constrained below the reach of seasonal frost, at approximately 15 m depth below the surface of the north face. This indicates that all permafrost on the mountain is relict, as defined by (Magnin et al., 2017), and survives only thanks to the thermal inertia of the ground. The model produces similar results for Nasaasaaq (Fig.10b), as for scenario RCP 2.6 we observe permafrost retreat to a point that the frozen body is below the reach of the seasonal frost on the whole south face. Scenario RCP 8.5 indicates that all permafrost on
440   the mountain is relict, except for the summit's north face.
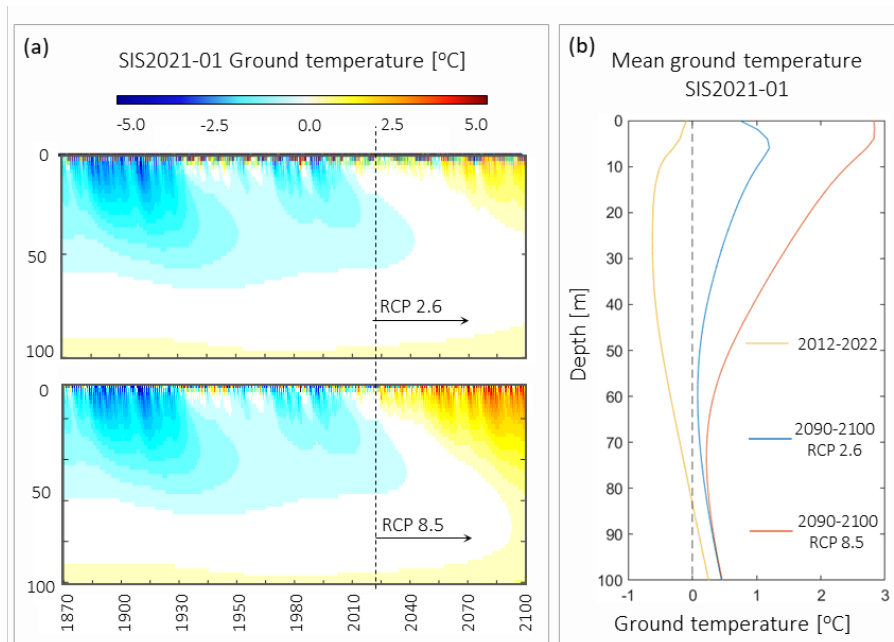
Figure 9. Summary of modeled evolution of temperatures at SIS2021-01. Temperature evolution over the period 1870-2100 depending on the different scenarios (a). Visualisation of temperature profiles as function of borehole depth for different periods and scenarios (b).

The common thread shown by these results is that the study area is going to experience a reduction in the extents of permafrost in rock walls by 2100, regardless the scenario considered. This due to the fact that permafrost in the area is discontinuous and already close to thawing point as of 2022. Even in scenario RCP 2.6, which causes a relatively mild increase in ATs compared to the current conditions, the numerical simulations forecast an increase of deep ground temperatures near 0°C at mid elevations (200 - 400 m.a.s.l.). This corresponds to the disappearance of permafrost in most low elevation south facing slopes. Scenario RCP 8.5 is expected to have a critical impact on the rock wall permafrost patterns in the area. While permafrost bodies may keep on existing below ground surface even at 200 m.a.s.l. (Fig.10a), less than 1% of the rock walls are expected to have a MRST below 0 °C by the end of the century, indicating that most rock wall permafrost in the area will become relict. Considering the strong temperature gradients between surface and deep rock temperatures (See RCP 8.5 on Fig.9b), it is arguable that even a stabilisation of the climate after 2100, the area will still experience a progressive decrease of rock wall permafrost extents.

These patterns of rock wall permafrost degradation are comparable to the expected evolution of rock wall permafrost at 3400 - 4000 m.a.s.l. in the French Alps described by Magnin et al. (2017). At their location, mountain permafrost is expected to retreat on the highest summits of the Mont Blanc massif, while only relict permafrost can persist at lower elevations. These findings imply that in the near future permafrost degradation will affect most of the rock walls in the Sisimiut area, creating the preliminary conditions for a possible increase in rockfall activity of both small and large magnitude (Krautblatter et al., 2013) as observed in the Mont Blanc massif (Ravanel and Deline, 2011).
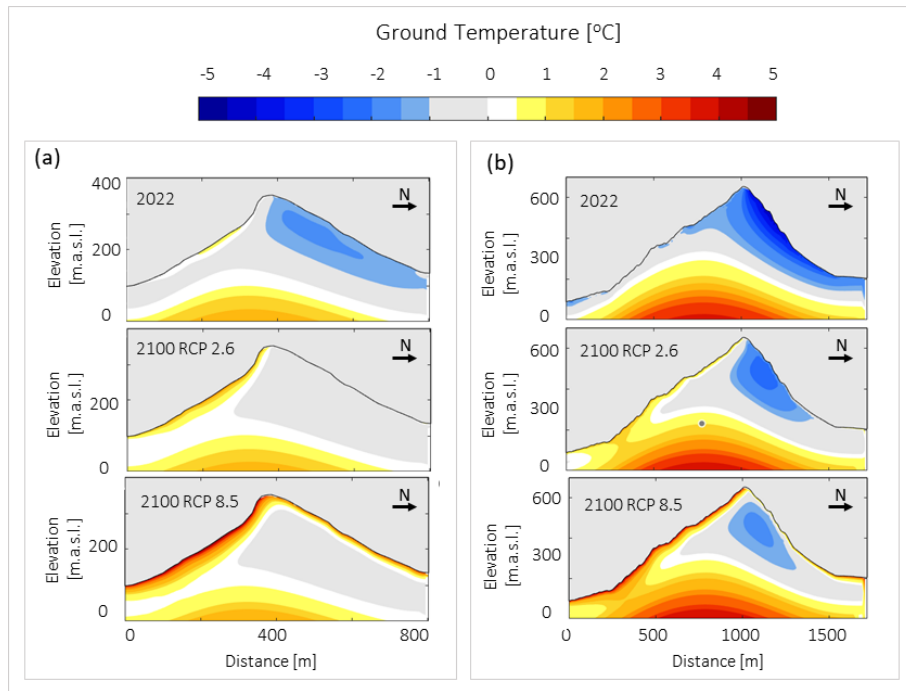
Figure 10. Summary of 2D simulations for future scenarios. 2D models are run until 2100 for RCP 2.6 and RCP 8.5 at the ERT location (a) and Nasaasaaq summit (b).

5   Conclusions

In this study, we investigate present rock wall permafrost conditions and their expected evolution across the 21st century in the Sisimiut area, West Greenland. Albeit localized in a small area, we have for the first time an assessment of rock wall permafrost conditions within the country. To describe rock wall permafrost here, we combine different data sources, including RST data, borehole temperatures, a ERT tomogram and regionally-available weather data. Rock temperatures are simulated using a combination of empirical and numerical models, applied both to 1D and 2D geometries. The main outcomes are the following:

– The modeling results consistently replicate the patterns described by the available data. The modeling uncertainties are of a similar order of magnitude to those observed in previous studies that employed identical methodologies in different geographic locations. This modeling approach is therefore suited to describe permafrost patterns in the study area.

– The data show widespread evidence of discontinuous permafrost in the area. Permafrost can be found in rock walls and bedrock already in shaded locations at sea level. South facing rock walls are observed to be permafrost free up to 400 m.a.s.l.. Measured permafrost temperatures are close to thawing point.

- Considering the optimistic scenario (scenario RCP 2.6), the model predicts a 9 % reduction of the extents of rock wall permafrost by the end of the 21st century. This will interest mostly the south faces, which will become permafrost-free at all elevations in the area. In this scenario, north faces may still host permafrost down to sea level.

- Considering the pessimistic scenario (scenario RCP 8.5), the model predicts a 99% reduction of the extents of rock wall permafrost by the end of the 21 st century. Permafrost will survive only in relict bodies at the core of summits below 600 m.a.s.l.. MRSTs are expected to be below 0 °C on north facing rock walls above 600 m.a.s.l..

- The current and future state of rock wall permafrost conditions in our study area closely resembles those described in the elevation range of 3300 to 4000 m.a.s.l. of the Mont-Blanc massif. Consequently, we hypothesize that this ongoing permafrost degradation forms the basis for an increase in rock fall and rock slide activity, as observed in Mont-Blanc area.

Although the correlation between permafrost degradation and rockfall activity is accepted within the scientific community (Ravanel and Deline, 2011; Patton et al., 2019), the process chain linking the two phenomena is very complex. Our modeling approach provides a good first assessment for rock wall permafrost zonation. Additional investigations of slope stability characteristics, and their relation to permafrost distribution and degradation could aid in the further refinement of the proposed modeling approach. For potentially endangered slopes this could be achieved by integrating high resolution snow distribution (Haberkorn et al., 2016) and crack networks (Magnin et al., 2020), providing a more detailed understanding of slope thermodynamics. Moreover, future research activities should aim at the application of the proposed modeling approach for investigations at larger scales.

Author contributions. MM designed the study, conducted fieldwork and modeling. PAD conducted geophysical fieldwork and data processing. ST participated in geophysical fieldwork. SRN organised deep boreholes drillings. AR advised on geophysical data processing. TIN supervised the study, field logistics and data interpretation. All authors contributed to the manuscript.

Competing interests. No competing interests are present

Acknowledgements. This study is part of project TEMPRA and Siku Aajiutsoq, funded by the Greenland Research Council. The study is also part of the Nunataryuk project, which is funded under the European Union's Horizon 2020 Research and Innovation Programme under Grant Agreement 773421. The deep boreholes were established as part of the Greenland Integrated Observing System (GIOS) funded by the Danish National Fund for Research Infrastructure (NUFI) under the Ministry for higher Education and Science. This work was realised in cooperation with EDYTEM and Styx4D. We acknowledge Jessy Lossel for his work on the rock samples.

References

(Springer Series in Statistics) Emanuel Parzen, Kunio Tanabe, Genshiro Kitagawa (auth.), Emanuel Parzen, Kunio Tanabe, Genshiro Kitagawa (eds.)-Selected Papers of Hirotugu Akaike-Springer-Verlag New.pdf.

Allen, S. K., Gruber, S., and Owens, I. F.: Exploring Steep Bedrock Permafrost and its Relationship with Recent Slope Failures in the Southern Alps of New Zealand, 356, 345–356, https://doi.org/DOI: 10.1002/ppp.658, 2009.

Bentsen, M., Bethke, I., Debernard, J. B., Iversen, T., Kirkevåg, A., Seland, Ø., Drange, H., Roelandt, C., Seierstad, I. A., Hoose, C., and Kristjánsson, J. E.: The Norwegian Earth System Model, NorESM1-M – Part 1: Description and basic evaluation of the physical climate, Geoscientific Model Development, 6, 687–720, https://doi.org/10.5194/gmd-6-687-2013, 2013.

Biskaborn, B. K., Smith, S. L., Noetzli, J., Matthes, H., Vieira, G., Streletskiy, D. A., Schoeneich, P., Romanovsky, V. E., Lewkowicz, A. G., Abramov, A., Allard, M., Boike, J., Cable, W. L., Christiansen, H. H., Delaloye, R., Diekmann, B., Drozdov, D., Etzelmüller, B., Grosse, G., Guglielmin, M., Ingeman-Nielsen, T., Isaksen, K., Ishikawa, M., Johansson, M., Johannsson, H., Joo, A., Kaverin, D., Kholodov, A., Konstantinov, P., Kröger, T., Lambiel, C., Lanckman, J. P., Luo, D., Malkova, G., Meiklejohn, I., Moskalenko, N., Oliva, M., Phillips, M., Ramos, M., Sannel, A. B. K., Sergeev, D., Seybold, C., Skryabin, P., Vasiliev, A., Wu, Q., Yoshikawa, K., Zheleznyak, M., and Lantuit, H.: Permafrost is warming at a global scale, Nature Communications, 10, 1–11, https://doi.org/10.1038/s41467-018-08240-4, 2019.

Brown, R. J. E.: The distribution of permafrost and its relation to air temperature in Canada and the U.S.S.R., Arctic, 13, 163–177, https://doi.org/10.14430/arctic3697, 1960.

Cappelen, J. and Jensen, D.: Climatological Standard Normals 1991-2020 - Greenland, Tech. rep., DMI - Danish Meteorological Institute, https://www.dmi.dk/publikationer/, 2021.

Cappelen, J., Vinther, B. M., Kern-Hansen, C., Laursen, E. V., and Jørgensen, P. V.: Greenland-DMI Historical Climate Data Collection 1784-2020, Tech. Rep. May, www.dmi.dkwww.dmi.dkurlhttps://www.dmi.dk/publikationer/www.dmi.dk, 2021.

Colgan, W., Rajaram, H., Abdalati, W., McCutchan, C., Mottram, R., Moussavi, M. S., and Grisby, S.: Glacier crevasses: Observations, models, and mass balance implications, Reviews of Geophysics, 54, 119–161, https://doi.org/doi:10.1002/2015RG000504, 2016.

COMSOL Inc.: COMSOL Multiphysics, Heat Transfer Module User's Guide, version 5.4, https://doc.comsol.com/5.4/doc/com.comsol.help.heat/HeatTransferModuleUsersGuide.pdf, 2015.

Coperey, A., Revil, A., and Stutz, B.: Electrical Conductivity Versus Temperature in Freezing Conditions: A Field Experiment Using a Basket Geothermal Heat Exchanger, Geophysical Research Letters, 46, 14531–14538, https://doi.org/10.1029/2019GL084962, 2019.

Czekirda, J., Etzelmüller, B., Westermann, S., Isaksen, K., and Magnin, F.: Post-Little Ice Age rock wall permafrost evolution in Norway, The Cryosphere, pp. 2725–2754, 2023.

Daanen, R. P., Ingeman-Nielsen, T., Marchenko, S. S., Romanovsky, V. E., Foged, N., Stendel, M., Christensen, J. H., and Hornbech Svendsen, K.: Permafrost degradation risk zone assessment using simulation models, Cryosphere, 5, 1043–1056, https://doi.org/10.5194/tc-5-1043-2011, 2011.

Dahlin, T. and Zhou, B.: A numerical comparison of 2D resistivity imaging with 10 electrode arrays, Geophysical Prospecting, 52, 379–398, https://doi.org/10.1111/j.1365-2478.2004.00423.x, 2004.

Delhasse, A., Kittel, C., Amory, C., Hofer, S., As, D. V., Fausto, R. S., and Fettweis, X.: Brief communication : Evaluation of the near-surface climate in ERA5 over the Greenland Ice Sheet, 5, 957–965, 2020.

Duvillard, P., Ravanel, L., Schoeneich, P., Deline, P., Marcer, M., and Magnin, F.: Cold Regions Science and Technology Qualitative risk assessment and strategies for infrastructure on permafrost in the French Alps, 2021.

535   Duvillard, P.-A., Magnin, F., Revil, A., Legay, A., Ravanel, L., Abdulsamad, F., and Coperey, A.: Temperature distribution in a permafrost-affected rock ridge from conductivity and induced polarization tomography, Geophysical Journal International, pp. 1207–1221, https://doi.org/10.1093/gji/ggaa597, 2020.

Etzelmüller, B.: Recent advances in mountain permafrost research, Permafrost and Periglacial Processes, 24, 99–107, https://doi.org/10.1002/ppp.1772, 2013.

540   Etzelmüller, B., Czekirda, J., Magnin, F., Duvillard, P. A., Ravanel, L., Malet, E., Aspaas, A., Kristensen, L., Skrede, I., Majala, G. D., Jacobs, B., Leinauer, J., Hauck, C., Hilbich, C., Böhme, M., Hermanns, R., Eriksen, H. O., Lauknes, T. R., Krautblatter, M., and Westermann, S.: Permafrost in monitored unstable rock slopes in Norway-New insights from temperature and surface velocity measurements, geophysical surveying, and ground temperature modelling, Earth Surface Dynamics, 10, 97–129, https://doi.org/10.5194/esurf-10-97-2022, 2022.

Fiddes, J. and Gruber, S.: TopoSUB: A tool for efficient large area numerical modelling in complex topography at sub-grid scales, Geosci-
545   entific Model Development, 5, 1245–1257, https://doi.org/10.5194/gmd-5-1245-2012, 2012.

Fiddes, J. and Gruber, S.: TopoSCALE v.1.0: Downscaling gridded climate data in complex terrain, Geoscientific Model Development, 7, 387–405, https://doi.org/10.5194/gmd-7-387-2014, 2014.

Frauenfelder, R., Isaksen, K., Lato, M. J., and Noetzli, J.: Ground thermal and geomechanical conditions in a permafrost-affected high-latitude rock avalanche site (Polvartinden, northern Norway), Cryosphere, 12, 1531–1550, https://doi.org/10.5194/tc-12-1531-2018, 2018.

550   Gallach, X., Carcaillet, J., Ravanel, L., Deline, P., Ogier, C., Rossi, M., Malet, E., and Garcia-Sellés, D.: Climatic and structural controls on Late-glacial and Holocene rockfall occurrence in high-elevated rock walls of the Mont Blanc massif (Western Alps), Earth Surface Processes and Landforms, 45, 3071–3091, https://doi.org/10.1002/esp.4952, 2020.

GAPHAZ: Assessment of Glacier and Permafrost Hazards in Mountain Regions - Technical Guidance Document, Prepared by Allen, S., Frey, H., Huggel, C. et al. Standing Group on Glacier and Permafrost Hazards in Mountains (GAPHAZ) of the International Association
555   of Cryospheric Sciences (IACS) and the International Permafrost Association (IPA). Zurich, Switzerla, p. 72, 2017.

Gruber, S.: Derivation and analysis of a high-resolution estimate of global permafrost zonation, Cryosphere, 6, 221–233, https://doi.org/10.5194/tc-6-221-2012, 2012.

Gruber, S., Hoelzle, M., and Haeberli, W.: Rock-wall temperatures in the Alps: Modelling their topographic distribution and regional differences, Permafrost and Periglacial Processes, 15, 299–307, https://doi.org/10.1002/ppp.501, 2004.

560   Guerin, A., Ravanel, L., Matasci, B., Jaboyedoff, M., and Deline, P.: The three-stage rock failure dynamics of the Drus (Mont Blanc massif, France) since the June 2005 large event, Scientific Reports, 10, 1–21, https://doi.org/10.1038/s41598-020-74162-1, 2020.

Haberkorn, A., Wever, N., Hoelzle, M., Phillips, M., Kenner, R., Bavay, M., and Lehning, M.: Distributed snow and rock temperature modelling in steep rock walls using Alpine3D, The Cryosphere Discussions, pp. 1–30, https://doi.org/10.5194/tc-2016-73, 2016.

Hersbach, H., Bell, B., Berrisford, P., Hirahara, S., Horányi, A., Muñoz-Sabater, J., Nicolas, J., Peubey, C., Radu, R., Schepers, D., Sim-
565   mons, A., Soci, C., Abdalla, S., Abellan, X., Balsamo, G., Bechtold, P., Biavati, G., Bidlot, J., Bonavita, M., De Chiara, G., Dahlgren, P., Dee, D., Diamantakis, M., Dragani, R., Flemming, J., Forbes, R., Fuentes, M., Geer, A., Haimberger, L., Healy, S., Hogan, R. J., Hólm, E., Janisková, M., Keeley, S., Laloyaux, P., Lopez, P., Lupu, C., Radnoti, G., de Rosnay, P., Rozum, I., Vamborg, F., Villaume, S., and Thépaut, J. N.: The ERA5 global reanalysis, Quarterly Journal of the Royal Meteorological Society, 146, 1999–2049, https://doi.org/10.1002/qj.3803, 2020.

570   Hilbich, C., Hauck, C., Hoelzle, M., Scherler, M., Schudel, L., Völksch, I., Vonder Mühl, D., and Mäusbacher, R.: Monitoring mountain permafrost evolution using electrical resistivity tomography: A 7-year study of seasonal, annual, and long-term variations at Schilthorn, Swiss Alps, Journal of Geophysical Research: Earth Surface, 113, 1–12, https://doi.org/10.1029/2007JF000799, 2008.

Hipp, T., Etzelmüller, B., and Westermann, S.: Permafrost in Alpine Rock Faces from Jotunheimen and Hurrungane, Southern Norway, Permafrost and Periglacial Processes, 25, 1–13, https://doi.org/10.1002/ppp.1799, 2014.

575 Isaksen, K., Lutz, J., Sørensen, A. M., Godøy, Ø., Ferrighi, L., Eastwood, S., and Aaboe, S.: Advances in operational permafrost monitoring on Svalbard and in Norway, Environmental Research Letters, 17, https://doi.org/10.1088/1748-9326/ac8e1c, 2022.

Keuschnig, M., Krautblatter, M., Hartmeyer, I., Fuss, C., and Schrott, L.: Automated Electrical Resistivity Tomography Testing for Early Warning in Unstable Permafrost Rock Walls Around Alpine Infrastructure, Permafrost and Periglacial Processes, 28, 158–171, https://doi.org/10.1002/ppp.1916, 2017.

580 Kneisel, C.: Assessment of subsurface lithology in mountain environments using 2D resistivity imaging, Geomorphology, 80, 32–44, https://doi.org/10.1016/j.geomorph.2005.09.012, 2006.

Krautblatter, M. and Hauck, C.: Electrical resistivity tomography monitoring of permafrost in solid rock walls, Journal of Geophysical Research: Earth Surface, 112, 1–14, https://doi.org/10.1029/2006JF000546, 2007.

Krautblatter, M., Verleysdonk, S., Flores-Orozco, A., and Kemna, A.: Temperature-calibrated imaging of seasonal changes in permafrost
585 rock walls by quantitative electrical resistivity tomography (Zugspitze, German/Austrian Alps), Journal of Geophysical Research: Earth Surface, 115, 1–15, https://doi.org/10.1029/2008JF001209, 2010.

Krautblatter, M., Funk, D., and Günzel, F. K.: Why permafrost rocks become unstable: A rock-ice-mechanical model in time and space, Earth Surface Processes and Landforms, 38, 876–887, https://doi.org/10.1002/esp.3374, 2013.

Legay, A., Magnin, F., and Ravanel, L.: Rock temperature prior to failure: Analysis of 209 rockfall events in the Mont Blanc massif (Western
590 European Alps), Permafrost and Periglacial Processes, 32, 520–536, https://doi.org/10.1002/ppp.2110, 2021.

Ljungdahl, B.: Geologisk oversigt: Grønland, 1967.

Loke, M. H. and Barker, R. D.: Rapid least-squares inversion of apparent resistivity pseudosections by a quasi-Newton method, Geophysical Prospecting, 44, 131–152, https://doi.org/10.1111/j.1365-2478.1996.tb00142.x, 1996.

Magnin, F., Deline, P., Ravanel, L., Noetzli, J., and Pogliotti, P.: Thermal characteristics of permafrost in the steep alpine rock walls of the
595 Aiguille du Midi (Mont Blanc Massif, 3842 m a.s.l), Cryosphere, 9, 109–121, https://doi.org/10.5194/tc-9-109-2015, 2015a.

Magnin, F., Krautblatter, M., Deline, P., Ravanel, L., Malet, E., and Bevington, A.: Determination of warm, sensitive permafrost areas in near-vertical rockwalls and evaluation of distributed models by electrical resistivity tomograph, Journal of Geophysical Research: Earth Surface, 120, 2452–2475, https://doi.org/10.1002/2014JF003351.Received, 2015b.

Magnin, F., Josnin, J. Y., Ravanel, L., Pergaud, J., Pohl, B., and Deline, P.: Modelling rock wall permafrost degradation in the Mont Blanc
600 massif from the LIA to the end of the 21st century, Cryosphere, 11, 1813–1834, https://doi.org/10.5194/tc-11-1813-2017, 2017.

Magnin, F., Etzelmüller, B., Westermann, S., Isaksen, K., Hilger, P., and Hermanns, R. L.: Permafrost distribution in steep slopes in Norway: measurements, statistical modelling and geomorphological implication, Earth Surface Dynamics Discussions, pp. 1–35, https://doi.org/10.5194/esurf-2018-90, 2019.

Magnin, F., Josnin, J., Magnin, F., Water, J. J., Permafrost, R., and Coupling, A.: Water Flows in Rockwall Permafrost : a Numerical Approach
605 Coupling Hydrological and Thermal Processes To cite this version : HAL Id : hal-03024087 Water Flows in Rockwall Permafrost : a Numerical Approach Coupling Hydrological, 2020.

Marcer, M., Stentoft, P. A., Bjerre, E., Cimoli, E., Bjørk, A., Stenseng, L., and Machguth, H.: Three Decades of Volume Change of a Small Greenlandic Glacier Using Ground Penetrating Radar, Structure from Motion, and Aerial Photogrammetry, Arctic, Antarctic, and Alpine Research, 49, 411–425, https://doi.org/10.1657/AAAR0016-049, 2017.

610 Myhra, K. S., Westermann, S., and Etzelmüller, B.: Modelled Distribution and Temporal Evolution of Permafrost in Steep Rock Walls Along a Latitudinal Transect in Norway by CryoGrid 2D, 182, 172–182, https://doi.org/10.1002/ppp.1884, 2017.

Noetzli, J. and Gruber, S.: Transient thermal effects in Alpine permafrost, Cryosphere, 3, 85–99, https://doi.org/10.5194/tc-3-85-2009, 2009.

Noetzli, J., Gruber, S., Kohl, T., Salzmann, N., and Haeberli, W.: Three-dimensional distribution and evolution of permafrost temperatures in idealized high-mountain topography, Journal of Geophysical Research: Earth Surface, 112, 1–14, https://doi.org/10.1029/2006JF000545, 615   2007.

Obu, J., Westermann, S., Bartsch, A., Berdnikov, N., Christiansen, H. H., Dashtseren, A., Delaloye, R., Elberling, B., Etzelmüller, B., Kholodov, A., Khomutov, A., Kääb, A., Leibman, M. O., Lewkowicz, A. G., Panda, S. K., Romanovsky, V., Way, R. G., Westergaard-Nielsen, A., Wu, T., Yamkhin, J., and Zou, D.: Northern Hemisphere permafrost map based on TTOP modelling for 2000–2016 at 1 km scale, Earth-Science Reviews, 193, 299–316, https://doi.org/10.1016/j.earscirev.2019.04.023, 2019.

620 Parr, C., Sturm, M., and Larsen, C.: Snowdrift Landscape Patterns : An Arctic Investigation, Water Resources Research, 56, https://doi.org/10.1029/2020WR027823, 2020.

Patton, A. I., Rathburn, S. L., and Capps, D. M.: Landslide response to climate change in permafrost regions, Geomorphology, 340, 116–128, https://doi.org/10.1016/j.geomorph.2019.04.029, 2019.

Pellet, C. and Noetzli, J.: Swiss Permafrost Bulletin 2018/2019, Permos 2020 (Swiss Permafrost Monitoring Network), pp. 1–20, 625   https://doi.org/10.13093/permos-2019-01.Cover, 2020.

Porter, C.: ArcticDEM, Version 3, 2018.

QGIS: QGIS Geographic Information System, QGIS.org. Last accessed September 2023, 2023.

Ravanel, L. and Deline, P.: Climate influence on rockfalls in high-alpine steep rockwalls: The north side of the aiguilles de chamonix (mont blanc massif) since the end of the 'Little Ice Age', Holocene, 21, 357–365, https://doi.org/10.1177/0959683610374887, 2011.

630 Rico, I., Magnin, F., López Moreno, J. I., Serrano, E., Alonso-González, E., Revuelto, J., Hughes-Allen, L., and Gómez-Lende, M.: First evidence of rock wall permafrost in the Pyrenees (Vignemale peak, 3,298 m a.s.l., 42°46′16′′N/0°08′33′′W), Permafrost and Periglacial Processes, pp. 673–680, https://doi.org/10.1002/ppp.2130, 2021.

Scandroglio, R., Draebing, D., Offer, M., and Krautblatter, M.: 4D quantification of alpine permafrost degradation in steep rock walls using a laboratory-calibrated electrical resistivity tomography approach, Near Surface Geophysics, 19, 241–260, 635   https://doi.org/10.1002/nsg.12149, 2021.

Schmidt, J. U., Etzelmüller, B., Schuler, T. V., Magnin, F., Boike, J., Langer, M., and Westermann, S.: Surface temperatures and their influence on the permafrost thermal regime in high Arctic rock walls on Svalbard, The Cryosphere, 15, 1–29, https://doi.org/10.5194/tc-2020-340, 2021.

Stocker-Mittaz, C., Hoelzle, M., and Haeberli, W.: Modelling alpine permafrost distribution based on energy-balance data: a first step, 640   Permafrost and Periglacial Processes, 13, 271–282, https://doi.org/10.1002/ppp.426, 2002.

Strzelecki, M. C., Jaskólski, M. W., and Strzelecki, M. C.: Arctic tsunamis threaten coastal landscapes and communities -Survey of Karrat Isfjord 2017 tsunami effects in Nuugaatsiaq, western Greenland, Natural Hazards and Earth System Sciences, 20, 2521–2534, https://doi.org/10.5194/nhess-20-2521-2020, 2020.

Svennevig, K.: Preliminary landslide mapping in Greenland, GEUS Bulletin, 43, 1–5, 2019.

645 Svennevig, K., Hermanns, R. L., Keiding, M., Binder, D., Citterio, M., Dahl-Jensen, T., Mertl, S., Sørensen, E. V., and Voss, P. H.: A large frozen debris avalanche entraining warming permafrost ground—the June 2021 Assapaat landslide, West Greenland, Landslides, 19, 2549–2567, https://doi.org/10.1007/s10346-022-01922-7, 2022.

Svennevig, K., Keiding, M., Korsgaard, N. J., Lucas, A., Owen, M., Poulsen, M. D., Priebe, J., Sørensen, E. V., and Morino, C.: Uncovering a 70-year-old permafrost degradation induced disaster in the Arctic, the 1952 Niiortuut landslide-tsunami in central West Greenland, Science of the Total Environment, 859, https://doi.org/10.1016/j.scitotenv.2022.160110, 2023.

Walls, M., Hvidberg, M., Kleist, M., Knudsen, P., Mørch, P., Egede, P., Taylor, G., Phillips, N., Yamasaki, S., and Watanabe, T.: Hydrological instability and archaeological impact in Northwest Greenland: Sudden mass movement events signal new concerns for circumpolar archaeology, Quaternary Science Reviews, 248, 106 600, https://doi.org/10.1016/j.quascirev.2020.106600, 2020.

Walter, F., Amann, F., Kos, A., Kenner, R., Phillips, M., de Preux, A., Huss, M., Tognacca, C., Clinton, J., Diehl, T., and Bonanomi, Y.: Direct observations of a three million cubic meter rock-slope collapse with almost immediate initiation of ensuing debris flows, Geomorphology, 351, 106 933, https://doi.org/10.1016/j.geomorph.2019.106933, 2020.

Westermann, S., Langer, M., Boike, J., Heikenfeld, M., Peter, M., Etzelmüller, B., and Krinner, G.: Simulating the thermal regime and thaw processes of ice-rich permafrost ground with the land-surface model CryoGrid 3, Geoscientific Model Development, 9, 523–546, https://doi.org/10.5194/gmd-9-523-2016, 2016.